

Solvothermal vapor annealing and environmental control setup with adjustable magnetic field module for GISAXS studies.

Christian Kjeldbjerg,¹ Bo Jakobsen,¹ Miriam Varón,² Kim Lefmann,³ Cathrine Frandsen,² and Dorthe Posselt^{*4}

¹IMFUFA, Department of Science and Environment, Roskilde University, DK-4000 Roskilde, Denmark

²Department of Physics, Technical University of Denmark, DK-2800 Lyngby, Denmark

³NanoScience Center, Niels Bohr Institute, University of Copenhagen, DK-2100 Copenhagen Ø, Denmark

⁴FRUSTMI, IMFUFA, Department of Science and Environment, Roskilde University, DK-4000 Roskilde, Denmark

(Dated: February 13, 2026)

A compact, modular environmental control and solvothermal vapor annealing chamber designed for maintaining a controlled atmosphere with regard to solvent humidity and temperature is presented. The setup allows *ex situ* and *in situ* grazing incidence small-angle X-ray scattering (GISAXS) investigations of thin film self-assembly and reorganization. Its modular slotting system enables stable reconfiguration, including the integration of an adjustable magnetic field module. The temperature is maintained via a water-based heating and cooling loop supplemented by resistive elements, and the solvent vapor environment is regulated using a commercial controlled mixing and evaporation unit. The performance of the setup is validated through measurements of fill and quench times together with magnetic field mapping with Gauss meter measurements and finite element simulations. Further, the versatility of the setup is demonstrated with four research examples using the chamber for solvothermal vapor annealing of block copolymer thin films together with lab-based *ex situ* and *in situ* GISAXS measurements. The portable new design offers robust environmental control and flexibility for advanced thin film investigations both in the lab and at large scale facilities. The design can be adapted for grazing incidence small-angle neutron scattering, GISANS.

I. INTRODUCTION

A well-defined sample environment with high precision control of relevant parameters during small-angle X-ray scattering in transmission geometry (SAXS) and in grazing incidence geometry (GISAXS) often requires control of the atmosphere in the sample chamber (e.g., vacuum, inert gas, a certain level of water or solvent humidity), and the sample temperature. Typical soft matter thin film samples, which are mounted in direct contact with the sample environment atmosphere, include for instance block copolymers (BCPs), liquid crystals, and stacked phospholipid bilayers. Liquid crystals, which exhibit temperature-dependent phase behavior, require high precision temperature regulation to capture transitions between mesophases, e.g., from nematic to smectic phases¹. Phospholipids, as found in biological membranes, undergo phase changes depending on the temperature and hydration level². BCPs require thermal control to study their microphase separation³. In addition to thermal and humidity control, magnetic BCP thin films and hybrid BCP/magnetic-nanoparticle films can be aligned by external magnetic fields integrated into the sample environment, resulting in ordered nanostructures such as cylinders⁴ and nanowires^{5,6}. Thin BCP films prepared by, e.g., spin coating typically have a number of kinetically trapped defects, hence calling for annealing of the structure. For many BCP samples, thermal annealing is slow and potentially harsh and does not offer a large degree of control of the ordering process. Solvent vapor annealing (SVA), on the other hand, has emerged as a versatile technique where setups of increasing sophistication beyond simple jar annealing (i.e., a closed container with a liquid reservoir) offer a large degree of control over the annealing process^{7–9}. Solvothermal vapor annealing (STVA), where the temperature of the SVA setup can be raised somewhat above room temperature, facilitates the formation of highly ordered BCP thin film structures both by reduc-

ing the glass transition temperature (T_g) of the BCP constituent polymers due to uptake of solvent and by enhancing the molecular mobility of the BCP. Various characterization and environmental control components are often added to SVA setups such as devices for spectral reflectometry^{10–21}, ellipsometry^{22–25}, and cooling/heating elements for STVA.^{13,23,24,26–30} Setups have also been developed for *in situ* GISAXS experiments at synchrotron facilities^{10,14,15,30–33} making real-time tracking of structural changes in the films possible.

In this paper, we present an environmental control and STVA setup designed for annealing experiments including *in situ* GISAXS studies at both synchrotron and laboratory sources. The setup has a flexible modular design enabling a high degree of control of the environmental conditions to which the sample is exposed, typically composition of sample chamber atmosphere, temperature and magnetic field. The setup presented in this paper is a complete redesign of a previous setup from our group³⁴ and has been developed to meet new requirements, including a higher degree of environmental control, a faster response time with regard to atmospheric changes and the possibility of applying a magnetic field. The new design is more stable and flexible with an increased ease of accessibility, for instance when changing the sample. The chamber design can be adapted for grazing incidence small-angle neutron scattering (GISANS) measurements, broadening its applicability to include neutron-based structural and magnetic investigations.

II. SOLVENT VAPOR ANNEALING AND ENVIRONMENTAL CHAMBER DESIGN

A. Basic principles

The STVA setup presented here is constructed mainly with the purpose of studying BCP thin films, the main experimental

techniques being atomic force microscopy (AFM) before and after annealing in the STVA chamber and GISAXS with the sample placed in the STVA chamber and annealing performed either before transfer of the STVA chamber (or the annealed sample alone) into the X-ray beam (*ex situ* GISAXS) or during annealing (*in situ* GISAXS).

Bulk BCP phase behavior is determined by the chemistry of the different polymers that make up the individual BCP blocks and are parametrized by the Flory-Huggins interaction parameter χ , and topological parameters. These are the relative size of the different blocks bonded together through covalent bonds; the overall size of the BCP; and the overall BCP architecture (e.g., linear or star BCPs^{3,35}). For low values of χ (or correspondingly high temperatures, $\chi \propto T^{-1}$), the BCP forms a disordered melt. Lowering the temperature results in a disorder-order transition, the so-called microphase separation, where the different blocks segregate as much as bonding constraints allow into separate microdomains forming an overall ordered structure such as lamellae; cylinders on a hexagonal lattice; spheres on a cubic lattice³; or more complex structures, e.g., gyroid or Frank-Kasper phases^{36,37}. For thin BCP films, additional parameters come into play, such as interaction with the substrate and the film thickness (commensurate or non-commensurate with the characteristic BCP microdomain size)³⁸. As detailed elsewhere^{8,9}, the SVA process relies on the uptake of solvent to screen polymer–polymer interactions leading to an effective reduction in χ together with a reduction in the glass transition temperature, T_g , due to the small solvent molecules effectively acting as plasticizers. When the thin film is exposed to solvent vapor, uptake of solvent results in swelling of the film. The swelling process is typically monitored through the swelling ratio, $SR(t)$, the ratio of the swollen film thickness, $d(t)$, at a given time t to the initial dry film thickness, d_0 :

$$SR(t) = \frac{d(t)}{d_0}, \quad (1)$$

Reorganization of the BCPs towards the thermodynamic equilibrium structure (in the swollen state) is a complex process characterized by several time- and length scales. When the desired structure and degree of order is reached, the thin film is dried. It can either be quenched by fast drying or allowed to slowly relax toward the dry equilibrium state. The details of the full process can be controlled and fine-tuned experimentally by choice of solvent (selective or non-selective for the different polymer blocks), solvent vapor pressure during annealing, swelling protocol, drying rate and annealing temperature. Sophisticated protocols involve the use of several solvents³⁹. In the following, we use 'relative humidity' or 'solvent humidity' to express the degree of wetness in the chamber atmosphere with respect to the relevant solvent vapor, i.e., the concentration of solvent gas in the total chamber gas with 100% referring to a chamber atmosphere saturated with the relevant solvent gas.

GISAXS allows for the probing of thin film structures along the film normal and laterally in the plane perpendicular to the film normal. This is achieved by the incident X-ray beam illuminating the sample at a grazing angle, $\alpha_i \sim 0.1^\circ$. This way, a large footprint ensures a large illuminated thin film volume.

The critical angle, α_c , of a given film material defines the angle above which the X-ray beam will begin to penetrate the material. For $\alpha_i < \alpha_c$ the full beam is reflected and is marked by an intense spot on the 2D detector behind the sample, positioned at an X-ray beam exit angle equal to α_i . A schematic of GISAXS scattering geometry can be found in Supplementary Material Fig. S1. A substrate is typically chosen to have a higher critical angle, α_{cs} , than the film material under study, $\alpha_{cs} > \alpha_c$, and three regimes are identified^{9,40,41}:

- $\alpha_i < \alpha_c$: Evanescence regime
- $\alpha_c < \alpha_i < \alpha_{cs}$: Dynamic regime
- $\alpha_i > \alpha_{cs}$: Kinematic regime

In the evanescent regime, only the outermost few nm of the film surface is probed by the evanescent wave penetrating into the film. In the dynamic regime, the beam illuminates the whole film interior, and correspondingly, reflection and refraction of the beam at interfaces must be taken into account, resulting in complex dynamical effects. The scattering parallel to the film surface, i.e., along q_y , (see Fig. 8a for an example) gives information on lateral film structuring and is interpreted using standard SAXS scattering theory, i.e., form and structure factors⁴². Scattering in the scattering plane, defined by the incoming and the specularly reflected beam i.e., along q_z , gives information on the electron density depth profile in the film. The quantitative interpretation of this part of the scattering is complex, requiring the use of the distorted Wave Born approximation⁴³. In the kinematic regime, when $\alpha_i > \alpha_{cs}$, the intensity of the reflected signal drops sharply and modeling of the scattered intensity is typically much simplified^{40,44}.

Examples of the use of GISAXS to characterize restructuring processes in thin films using the STVA setup either *ex situ* or *in situ* are given at the end of the paper. First, we list the design criteria and describe the new design of the STVA setup while emphasizing the differences compared to our previous setup³⁴. The setup is then characterized with respect to filling the STVA chamber with solvent gas (swelling) and inert gas (drying), respectively, and the magnetic field available during STVA is characterized.

B. STVA chamber design criteria

The STVA setup consists of four modules: 1) the STVA chamber with accompanying exchangeable modular drawers, 2) a system for solvent vapor and nitrogen gas delivery, 3) a UV cell for measurement of solvent vapor concentration in the chamber exhaust gas (SVC), and 4) a commercial UV-VIS-NIR light spectral reflectometer for *in situ* measurements of the thin film thickness.

The STVA chamber is designed to meet the following criteria:

1. **GISAXS compatibility:** The chamber must be suitable for both laboratory-based and synchrotron GISAXS. It must be portable and lightweight and possible to mount

on a goniometer allowing control of α_i with high precision ($\pm 0.002^\circ$), tilt of the sample around the X-ray beam axis and possibly also rotation around the sample normal, both with high precision.

2. **Real-time thickness tracking:** It should be possible to connect the optical fiber of an UV-VIS-NIR spectral reflectometer to a chamber window in a stable and reproducible way, thus separating the fiber-optics from a potentially harsh atmosphere in the sample chamber and allowing reliable *in situ* film thickness tracking.
3. **Small sample chamber:** The chamber should have a compact design with a small free volume to allow fast environmental changes during solvent treatment and drying of thin films.
4. **Sample table and gas inlet:** The chamber should be equipped with a sample table that allows stable sample mount and gas inlet in a well-defined way (in time and space), with respect to all parts of the sample surface.
5. **Temperature control:** It must be possible to heat and cool the sample and maintain high-precision temperature control during the *in situ* experiments.
6. **Magnetic field compatibility:** The chamber should allow the sample to be mounted in a magnetic field with well-defined direction relative to the sample normal thus enabling studies involving magnetically sensitive materials.

The STVA chamber is constructed with stability and ease of access in mind. This has led to a drawer design that allows easy sample change by inserting a drawer with the sample table into a slot on the side of the chamber - see Fig. 1. This modular approach enables the option of changing the sample environment by changing the design of the drawer that goes into the slot. A Viton O-ring sits between the drawer back-plate and the chamber house and is held in place with four brass thumb screws, ensuring a tight seal. The drawers and chamber housing are CNC-machined from aluminum, making them solvent resistant and non-magnetic to not influence the magnetic fields generated by permanent magnets installed in one of the drawers available for experiments. The chamber is insulated on all six sides using Vekaplan-S rigid PVC foam insulation sheets held in place by plastic screws. Fig. 1 shows photos of the base drawer (1a), the magnetic drawer (1b), the underside of the base drawer (1c) together with the chamber housing with insulation sheets (1d). The base drawer has a sample table of $75 \times 20 \text{ mm}^2$ that allows STVA of multiple samples simultaneously, while the magnetic drawer has a sample table of $22 \times 22 \text{ mm}^2$. Both drawers have a mixing cavity on the backside, as shown in Fig. 1c, where gas is let in before entering the chamber proper through a number of holes evenly distributed on either side of the sample stage. This design promotes a uniform distribution of the gas around the sample and ensures that all parts of the sample are exposed to vapor at the same time without any delays between the different sides of the sample (as observed in very early versions of STVA setups

with gas inlet on one side). The magnetic drawer has room for an array of NdFeB permanent bar magnets on either side, each of which can be replaced by an aluminum dummy. By changing the orientation of the magnets both in-plane and out-of-plane field directions with respect to the sample surface can be produced. The compact design of the cell makes exchange of chamber gas faster than in our previous STVA setup³⁴ - see Tab. I. The current version has a free volume of $\sim 92 \text{ cm}^3$ with the base drawer and $\sim 45 \text{ cm}^3$ with the magnetic drawer while the older chamber had a volume of $\sim 375 \text{ cm}^3$. Kapton windows ($\sim 50 \mu\text{m}$), on each side of the chamber allows for *in situ* X-ray measurements. Supplementing (e.g., positioned below the Kapton windows), or substituting the X-ray transparent windows with sub-mm thick aluminum windows will allow the same STVA setup to be used for GISANS experiments. It may be advantageous to use a sample table which allows larger sample areas for neutron scattering than typically used for the X-ray scattering version. The chamber can also be used for transmission SAXS with the sample mounted upright on the sample table using a sandwich holder with a suitable large base allowing stable upright positioning.

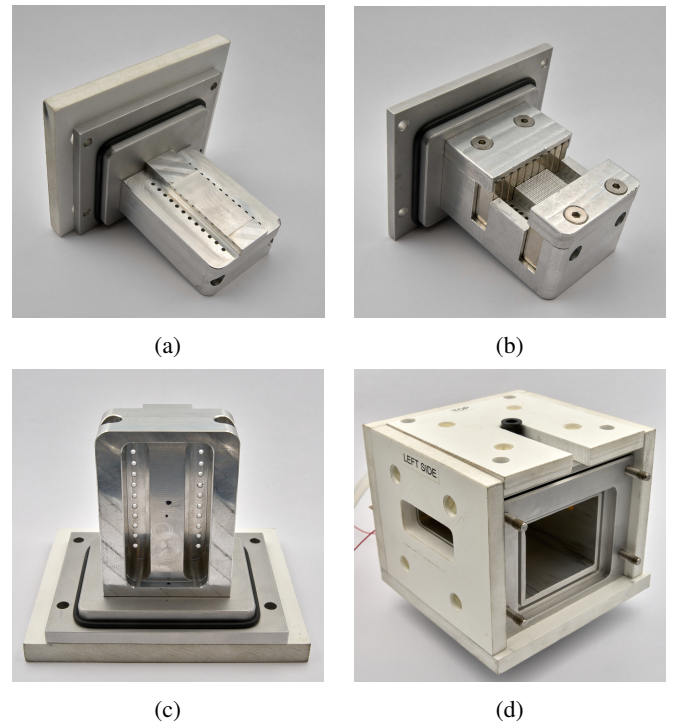


Figure 1: (a) Base drawer with large sample stage, (b) Magnetic drawer featuring a smaller sample stage designed for integrating permanent magnets, seen installed here on either side of the sample stage, to produce adjustable in-plane and out-of-plane fields, (c) Underside of base drawer featuring a mixing cavity for the incoming vapor and d) Chamber housing covered in insulation sheets and displaying the side with the opening where drawers are slotted in. An X-ray transparent window made of Kapton is also seen on the figure.

A water cooling / heating loop is drilled inside the base of the chamber and is connected to a Julabo DYNEO DD-200F

circulator via insulated tubing. Two resistive heating elements (Polyimide Thermo-foil Heater, 65 W, Minco Co.) located on the sides of the chamber allows for enhanced heating capability. A temperature probe (PT100) is glued directly to the chamber wall for temperature measurement and regulation. The chamber is designed for use with the surrounding atmosphere at ambient pressure.

C. Controlled evaporation and mixing system

The solvent gas is produced using a commercial controlled evaporation and mixing (CEM) system from Bronkhorst High-Tech B.V. The CEM consists of an evaporator (CEM Evaporator W-102 A) together with a mini CORI-FLOW 20 g/h Coriolis liquid flow meter to generate solvent vapor at specified humidity, temperature and flow rate. The overall setup is composed of 3 main components:

1. A liquid solvent reservoir is held in a 250 ml Borosilicate glass container (Duran pressure plus+ to safely maintain pressures up to \sim 1.5 bars) connected to a nitrogen gas inlet which supplies \sim 0.7 bar overpressure. Through pressurization of the reservoir, a pure liquid solvent stream is extracted and transferred to the CEM mixing valve.
2. The Coriolis liquid flow meter (20 g/h mini CORI-FLOW Bronkhorst High-Tech B.V.) measures and controls the liquid flow into the CEM mixing valve. The mixing valve controls the injection of a small amount of liquid into the steady carrier nitrogen gas flow of up to 200 sccm (cm^3 per minute at standard temperature and pressure), supplied by a mass flow controller from Bronkhorst (MFC). The resulting aerosol is then transferred to the evaporator.
3. The liquid-gas aerosol is evaporated in the temperature-controlled evaporation chamber of the CEM. The resulting gas mixture then passes through a tube into the STVA chamber.

The liquid flow through the flow meter is regulated together with the temperature of the evaporation chamber to obtain the desired solvent concentration (humidity), gas flow into the STVA chamber and final temperature of the gas mixture. The required set point liquid flow is calculated using an online software (FLUIDAT, from Bronkhorst). Henceforth, all relative humidities quoted for nitrogen–solvent mixtures correspond to the values calculated using FLUIDAT. By setting the temperature in the evaporation chamber slightly higher than the target temperature, condensation in the connecting tubes is avoided. A second MFC is connected to the STVA chamber via a separate inlet and can supply up to 400 sccm nitrogen flow during drying.

D. Solvent vapor concentration unit and spectral reflectometer

The working principle of the SVC unit for tracking solvent concentration in the exhaust gas from the STVA chamber is as follows: The exhaust gas flows through a cell, where a mercury lamp providing 254 nm UV radiation illuminates a photodetector placed at the opposite end of the cell. The resulting absorbance of the exhaust gas, A , is calculated as:

$$A = -\log_{10} T = -\log_{10} \frac{I}{I_0}, \quad (2)$$

where the transmittance, $T = I/I_0$, is the ratio between the UV intensity, I , transmitted through the solvent containing exhaust gas, and the intensity, I_0 , transmitted through pure nitrogen exhaust gas. The SVC unit works with solvents absorbing 254 nm UV light, typically solvent molecules with π -bonding, e.g., toluene or acetone.

Building on our previous design³⁴, the SVC unit has now been upgraded to include temperature control. A heating wire heats the SVC cell to avoid condensation of solvent inside the cell during SVA. The SVC unit is operated by remote control from a computer outside the experimental area via a microcontroller (Arduino SA) connecting to a PT100 temperature probe attached to the cell housing.

We use a UV-VIS-NIR commercial spectral reflectometer (NanoCalc-XR, Ocean Optics Ltd.; repeatability 0.3 nm) to continuously monitor film thickness during swelling and drying. The fiber-optic probe is mounted on top of the STVA chamber, directing light through a sapphire window onto the sample table surface at the standard position of the thin film sample. In the current setup, samples are loaded through the side of the STVA chamber, in contrast to the former design, where the loading took place through the top part where the fiber-optics are mounted. With the new design we have improved the stability and the reproducibility of the thickness measurements. The sample-probe distance can be adjusted to optimize the reflected intensity enabling the accommodation of various substrate thicknesses and sample stage heights. Calibration is performed by providing the spectrum from a reference sample, typically a bare Si wafer, and a dark measurement i.e. a measurement of any stray reflections originating in the light optical path. The dark measurement is performed by covering the sample stage with a piece of IR flock sheet (Musou Black USA, Costa Mesa, CA, USA), which has a reported 0.3% average reflectance in the visible spectrum thus largely ensuring that only internal reflections are sampled during calibration. Finally, a polystyrene thin film sample with known thickness is used as a standard sample for checking the thickness measurement setup. Analysis of the measured reflectance requires a model for the film measured in terms of the number of layers in the film with thickness and refractive index for each layer⁴⁵.

E. Integration into a laboratory-based GISAXS setup

At RUCA SAXS (Roskilde University Interdisciplinary X-ray Scattering Hub), the STVA chamber is housed within the main

sample environment enclosure of a XEUS 3.0 UHR XL instrument (Xenocs, Grenoble, France), an advanced system designed for wide- and small-angle X-ray scattering experiments (see Fig. 2a). The STVA chamber is mounted on a goniometer with two translational motors for sample positioning in the horizontal y -direction and the vertical z -direction, respectively (see Fig. 2b). Rotational motors allow adjustment of the incident beam angle, α_i , for GISAXS measurements and likewise, the sample can be tilted around the beam axis for alignment.

The CEM and MFC are positioned outside the main sample environment enclosure, with flow tubing directed into the STVA chamber through ports in the main enclosure walls. Before exiting the main enclosure, the exhaust gas passes through the SVC unit before ultimately being discharged through the laboratory exhaust system. Water tubes between the STVA chamber and the Julabo circulator use the same main enclosure exit port, with tubing lengths kept minimal to reduce temperature gradients. Foam padding on the water pipes outside the main enclosure further mitigates temperature fluctuations. Experiments are performed at ambient pressure in the main enclosure which requires the detector tank vacuum to be separated from the main enclosure by cap with a Kapton window (thickness $\sim 75 \mu\text{m}$) to allow passage of scattered X-rays (see Fig. 2a).

The reflectometer fiber-optic probe extends from the top of the STVA chamber and is loosely mounted along the top of the enclosure leading to an exit port thus minimizing strain on the optic fiber during sample alignment. The spectral reflectometer is positioned outside the main enclosure next to the CEM system.

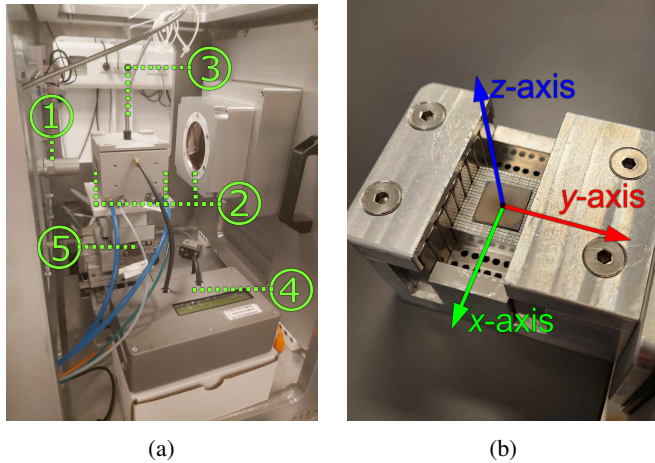


Figure 2: Photographs of the STVA chamber mounted inside the RUCSAXS sample-environment enclosure. (a) Overview with key components labeled: (1) X-ray beam from source, (2) Kapton windows in the beam path, (3) fiber-optic probe, (4) SVC unit, and (5) linear and rotary motion stage. (b) Sample mounted on the magnetic drawer stage, with axes annotated: the x and y directions lie in the sample plane, with x along the beam direction, while z is normal to the sample surface (out of plane).

Typical slit sizes defining the beam geometry for GISAXS are 0.04 mm vertically and 0.4 mm horizontally. In case of weakly scattering samples, this may be relaxed somewhat, e.g., 0.1 mm vertically and 0.5 mm horizontally, but with attention to the sample size and hence the maximal footprint on the sample. To start the GISAXS alignment, the sample stage is first translated in the horizontal (x) direction along the beam and then in the vertical (z) direction while the detector records the total photon signal (see Fig. 2b for axis orientation). Sudden changes in the total number of counts reveal at which positions the beam enters and leaves the sample surface (footprint). In case of the RUCSAXS setup with an Eiger 2R 1M detector (Dectris, Baden, Switzerland), no beam stop is needed to protect the detector. With the sample located, height, z , and the incident angle, α_i , are refined in an alternating procedure, while the two settings are strongly coupled. A scan in z identifies the surface height at the half-maximum intensity point, and, at that height, a scan of α_i finds the position where the direct-beam intensity, as defined by a rectangular region of interest on the detector, is at its maximum. This angle is defined as the zero incoming angle to be fine-tuned in the following procedure. The z and α_i settings are coupled and the scans are repeated twice more with progressively smaller step sizes and narrower ranges to fine-tune the alignment. Finally, α_i is raised to an angle between 0.1° and 0.18° , a value which is below the critical angle for penetration of the (Si) substrate, but still large enough to provide a strong specular reflection separated from the direct beam on the detector. Any mismatch between the observed and geometrically expected reflection position is checked with a custom-made plotting routine and corrected by an adjustment of α_i within $\pm 0.0025^\circ$. This uncertainty is linked to the estimate of the sample-to-detector distance and hence also to the size of the beam footprint on the sample, especially at low sample-to-detector distances. The procedure is typically executed for two different incoming angles, e.g., 0.11° and 0.17° .

III. EVALUATION AND OPTIMISATION

In this section, the operational parameters of the environmental chamber are assessed, including gas exchange times, magnetic field control, and performance during X-ray scattering experiments.

A. Fill and quench of chamber

During annealing a certain protocol is followed where it is important to establish a new solvent vapor pressure in the annealing chamber as fast as possible. Likewise, in order to maintain a nanostructure obtained by solvent vapor annealing of block copolymers, fast drying (quench) times are often desirable¹³. Because the characteristic filling or emptying time scales with the internal free volume, a smaller chamber is advantageous. The absorbance in the exhaust gas is proportional to the solvent-vapor concentration. Following a step-change in inlet gas humidity during filling, this absorbance increases

according to

$$A(t) = A_\infty \left[1 - e^{-t/\tau} \right], \quad (3)$$

and for a quench with dry gas, the absorbance decays as

$$A(t) = A_0 e^{-t/\tau}, \quad (4)$$

where $A(t)$ is the absorbance, A_∞ is the final steady-state absorbance during filling reached after a long time, $A_0 \equiv A(t=0)$ is the absorbance at the onset of a quench, and chamber volume, V , divided by gas flow, Q , V/Q , is the theoretical residence time constant, τ_{th} . The base drawer ($V = 92 \text{ cm}^3$, $Q = 200 \text{ sccm}$) gives $\tau_{\text{th}} = 27.6 \text{ s}$, while the magnetic drawer ($V = 45 \text{ cm}^3$, $Q = 200 \text{ sccm}$) gives 13.5 s (Tab. I). During filling, the time required for $A(t)$ to change from 10% to 90% of A_∞ is $\Delta t_{10 \rightarrow 90} = \tau_{\text{th}} \ln 9 \approx 2.20 \tau_{\text{th}}$. We extract two characteristic times from each experimental absorbance curve in Fig. 3: (i) a time constant from an exponential fit, τ_{fit} , and (ii) the 10–90% window $\Delta t_{10 \rightarrow 90} = t_{90\%} - t_{10\%}$ (or $t_{10\%} - t_{90\%}$ for a quench), read directly from the curve. The ratio $\Delta t_{10 \rightarrow 90} / (2.20 \tau_{\text{fit}})$ stays within $\pm 15\%$.

Parameter	Magnetic drawer	Base drawer
Free volume	45 cm^3	92 cm^3
$\Delta t_{10 \rightarrow 90}$ (200 sccm fill)	40.9 s	58.9 s
τ_{th} (200 sccm fill)	13.5 s	27.6 s
τ_{fit} (200 sccm fill)	16.5 s	25.6 s
$\Delta t_{90 \rightarrow 10}$ (600 sccm quench)	27.3 s	38.3 s
τ_{th} (600 sccm quench)	4.5 s	9.2 s
τ_{fit} (600 sccm quench)	12.7 s	19.0 s

Table I: Free volume and characteristic fill/quench times for magnetic drawer and base drawer. τ_{fit} values are obtained from fitting exponential models to the experimental absorbance curves; $\Delta t_{10 \rightarrow 90}$ and $\Delta t_{90 \rightarrow 10}$ are read directly from the absorbance curves.

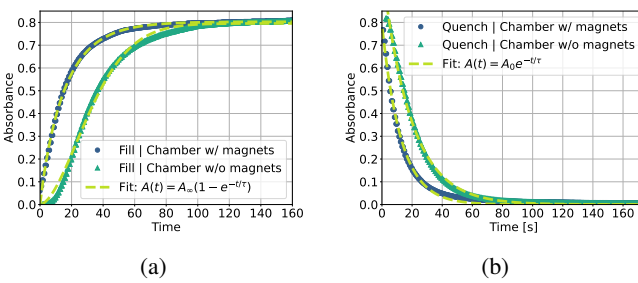


Figure 3: (a) The absorbance as function of time during chamber filling with fits to eq. 3 for both magnetic and base drawer. (b) The absorbance as function of time and fits to eq. 4 during quenching.

For the 200 sccm fill, τ_{fit} differs from τ_{th} by less than 20%. During the 600 sccm quench, however, τ_{fit} is two-to-three times larger, likely because additional condensed solvent must evaporate from interior walls, tubing, and seals before the

chamber is truly dry. Compared with our previous setup³⁴, the characteristic filling and emptying times are reduced by a factor of 5–10, as expected based on the change in chamber volume.

B. Application of a magnetic field during STVA

The compact size of the STVA chamber, and therefore the size of the slot for inserting a sample table drawer, limits the available volume for the inclusion of permanent magnets: a $10 \times 30 \times 5 \text{ mm}^3$ space on each side of the sample is available for this purpose. A magnetic field is generated by inserting up to $10 \times 10 \times 5 \text{ mm}^3$ N40 NdFeB permanent magnets, magnetized along the 5 mm axis, purchased from magnets4you GmbH. The magnets, up to 10 stacked together on either side of the sample table with their magnetization direction parallel to each other, can be aligned in different ways with the resulting field at the chamber table center either in the plane of the sample or parallel to the sample normal. In case of in-plane field (x-config., see Supplementary Material Fig. S2b), the field strength in the x-direction (along the X-ray beam path, cf. Fig. 2b) was measured by a Gauss meter 9 mm above the sample plane where the Hall element of the probe tip is located (cf. Supplementary Material Fig. S2a). The measured field strengths above the sample center ($x, y, z = (0, 0, 9 \text{ mm})$) and edges ($\pm 11 \text{ mm}, 0, 9 \text{ mm}$) are plotted as grass-green markers in Fig. 4 versus the number of magnets inserted. When the full 2×10 magnet array is in place, the two traces merge, indicating that the in-plane magnetic field achieves optimal homogeneity along the X-ray beam when the array is complete. Potential lateral variations in field strength along the y-axis (perpendicular to the beam in the sample plane) were not investigated in this study.

The drawer is optimized for producing a field along the X-ray beam path (x-config.), but the field can be directed out-of-plane along z by rotating the magnetic bar arrays into a vertical orientation (rotation about the x -axis). In this z-config. arrangement, using up to six magnets per side yields $B_z \approx 120 \text{ mT}$ at the stage center and about 100 mT near the edges. Rotating the bar arrays by 90° within the sample (film) plane brings opposite poles face-to-face across the 22 mm gap between the magnets, so the field is redirected into y-config. and inherently amplified, along y . Further increases are possible using thicker bar magnets, yet ultimately constrained by the drawer clearance of $10 \times 30 \times 50 \text{ mm}^3$ around the sample. A schematic overview of the three orthogonal field geometries is available in Supplementary Material Fig. S2b.

To further analyze the magnetic field distribution, we simulated the experimental setup using the package Elmer⁴⁶, a finite element method (FEM) solver. The simulation focused on a magnet array in air corresponding to the one used in the STVA setup, but neglecting the aluminum STVA chamber and sample stage in order to simplify the model. The magnets were modeled as blocks with specified remanent flux density based on N40 NdFeB values from the vendors website⁴⁷, $B_r = 1.3 \text{ T}$. The surrounding air was modeled using the vacuum permeability, μ_0 . The results, presented in Fig. 4 (light

green), validate the experimental findings (grass-green), showing good agreement in field strengths 9 mm above the sample stage center and the edges for all numbers of magnets inserted, though with a notably larger maximum relative deviation at the edges (80%) than at the center (6%). The FEM analysis also revealed the field distribution beyond the measurement range of the Gauss probe, namely at the level of the sample position at $(x, y, z) = (0, 0, 0 \text{ mm})$ and $(x, y, z) = (\pm 11 \text{ mm}, 0, 0 \text{ mm})$ (dark-blue curves).

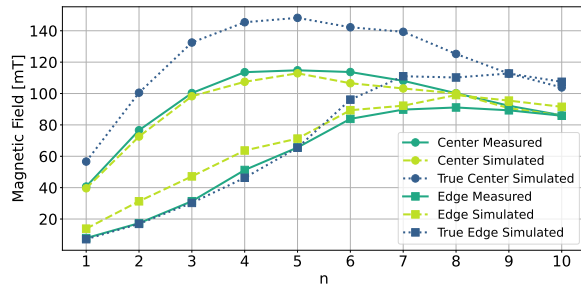


Figure 4: Magnetic field magnitude in mT measured with a Gauss probe (solid lines) and computed by FEM (dashed lines) at a height of $z = 9 \text{ mm}$ above the sample stage, plotted versus the number of magnets (n) inserted on each side of the stage. Center values correspond to $(x, y) = (0, 0)$ and edge values to $(x, y) = (\pm 11 \text{ mm}, 0)$. Circle markers denote center data and square markers edge data.

The full magnetic field landscape at the sample stage position as simulated with FEM is shown in Supplementary Material Fig. S2c. From this analysis we estimate the in-plane field within an area of $20 \times 20 \text{ mm}^2$ of the sample stage (corresponding to a typical sample size) to be slightly higher than 100 mT with all 2×10 permanent magnets inserted.

C. Stability of reflected X-ray beam

When testing *in situ* GISAXS during STVA of polymer thin films, the position of the reflected beam on the detector was observed to show large variations during use of large relative solvent humidities ($>70\%$) at room temperature. By placing the sample on a sanded aluminum plate of a size similar to the sample or by placing the sample on 3 small shards of Si wafer, the reflected beam position became stable. We conclude that the original smoothness of the sample stage allows for solvent to become trapped between sample and sample table via capillary forces resulting in a change of the angle of incidence and hence a change in exit angle of the reflected beam. As the solvent humidity in the chamber changes, so does the amount of solvent trapped and hence the position of the reflected beam on the detector varies with time in an unpredictable and non-reproducible way. The final sample table has thus been machined with a square pattern featuring a periodicity of 1 mm (cf. Supplementary Material Fig. S3), which has successfully eliminated problems with unstable beam angles relative to the sample surface.

IV. RESEARCH EXAMPLES

We present four examples highlighting the versatility of the STVA setup for thin film studies. The examples span magnetic field-driven nanoparticle assembly, morphological transformations in BCPs under controlled solvent atmosphere and at different temperatures and a demonstration of *in situ* GISAXS with a lab-based instrument. All polymers used were purchased from Polymer Source Inc. (Quebec, Canada); all polymer solutions were passed through $2 \mu\text{m}$ PTFE filters and used without further purification. Single-side-polished Si(100) wafers from Topsil GlobalWafers (Frederikssund, Denmark) served as substrates and were used as received unless stated otherwise. Polymer thin films were made by spin coating polymer solutions in toluene onto Si substrates at 3000 rpm with an acceleration of 4000 rpm s^{-1} .

A. Magnetic field-driven nanoparticle assembly in a block copolymer thin film template during STVA

The setup allows STVA under the application of a magnetic field as demonstrated with a system of magnetic $\gamma\text{-Fe}_2\text{O}_3$ nanoparticles dispersed in a block copolymer thin film during solution coating. The magnetic nanoparticles are coated with a thin polymer layer with the aim of rendering the particles preferentially miscible with one of the polymers in the BCP^{48–50}. In this particular experiment, the BCP is a polystyrene-*b*-polybutadiene diblock copolymer (PS-*b*-PB) while the magnetic nanoparticles are coated with PS. PS-*b*-PB has distinct mechanical properties at RT, where the minority block PS is in the glassy state (the glass transition temperature of PS is around 100°C) and expected to be forming PS cylinders³ in a matrix of the majority block, PB, which is in the rubber state (glass transition temperature of PB is typically around -85°C). The $\gamma\text{-Fe}_2\text{O}_3$ particles are synthesized following the procedure in Ref. 51 and measured by transmission electron microscopy to have a diameter of $10.2 \pm 2.7 \text{ nm}$ prior to coating with PS (cf. Supplementary Material Figs. in S4). To prepare the hybrid film, we first prepare a mixture of $100 \mu\text{l}$ 3 wt% PS(89.6)-*b*-PB(226), where the numbers in parentheses denote the number-average molecular weight M_n in kg mol^{-1} , with a polydispersity (PDI) of 1.05, and $50 \mu\text{l}$ PS-coated 1 wt% $\gamma\text{-Fe}_2\text{O}_3$ nanoparticles, both dispersed in toluene. Solution coating is performed by pipetting $40 \mu\text{l}$ of the mixture onto a Si wafer ($15 \times 15 \text{ mm}^2$), situated on the sample stage of the drawer with 10 magnets inserted on either side in the parallel magnetic field configuration. The drawer is slotted into the STVA chamber and a flow of 200 sccm 80% or nominally 100% toluene-saturated nitrogen (in praxis slightly undersaturated) is established. The film is left to dry in the toluene atmosphere at 24°C for at least 2 h after which the chamber is flushed with 600 sccm dry nitrogen.

The progress of the drying of the droplet is tracked by mounting the STVA chamber in the RUCSAXS experimental chamber and using the X-ray beam to scan along the height of the droplet. The position of the droplet-gas interface is found as the halfway point of the X-ray transmission curve. Fig. 5

shows how the 3 samples that were exposed to a lower concentration of toluene gas had a significantly increased drying rate averaging at 0.45 mm/h compared to the sample exposed to the highest possible concentration of toluene gas during drying where the evaporation rate was 0.13 mm/h. The drying rates are found by linear fits to the experimental data as shown in Fig. 5.

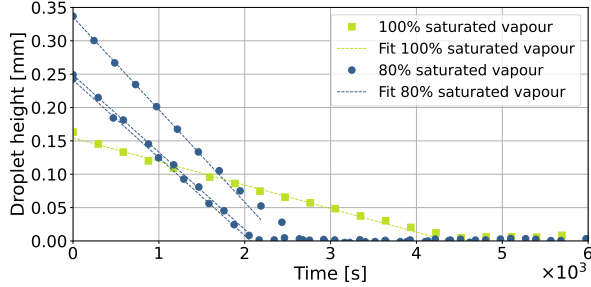


Figure 5: Evaporation rates of BCP/nanoparticle solution droplets left to dry in the STVA chamber with 80% or nominally 100% toluene-saturated nitrogen flow, as recorded from the halfway point of an X-ray scan along the droplet normal. Also shown are linear fits (dashed lines) to the data (filled dots or squares)

Optical microscopy images from the dried samples are shown in Figs. 6a and 6b. The images show clear wire-like structures formed along the direction of the applied field. Furthermore, comparison between samples formed with different rates of drying, reveal that slower drying allow the nanoparticles more time to form longer and thicker nanoparticle aggregates. The wire widths in Fig. 6 are in the few-micron regime, and for the nominally 100% toluene humidity case produces a higher density of wires >1 mm in length, while the 80% case more frequently forms shorter, oblong aggregates at this resolution. Large-area microscopy images are provided in the Supplementary Material (Figs. S5a,b), together with an image of a control sample prepared without application of a magnetic field during drying showing no apparent structure formation (Supplementary Material Fig. S5c). Supplementary Material Figs. S5d,e show analogous drying experiments performed on PS and PB homopolymer films with the same nanoparticle loading. In PS, the nanoparticles show only very limited formation of linear assemblies, whereas the PB film exhibits pronounced cracking and film delamination, consistent with PS-coated nanoparticles being incompatible with PB and thus no longer remaining embedded in the PB matrix.

AFM-phase images of films dried in an atmosphere of nominally 100% toluene humidity with and without a parallel magnetic field applied during drying are shown in Fig. 7. The glassy and rubbery phases in the BCP yields high contrast in AFM-phase imaging. Hence, from Fig. 7a it is evident that when no field is applied, the nanoparticle/BCP mixture has no tendency to form ordered elongated structures, while Fig. 7b demonstrates that such linear assemblies are formed when a magnetic field is applied during drying.

This behavior is consistent with the PS-coated nanoparticles preferentially partitioning into PS domains during solvent

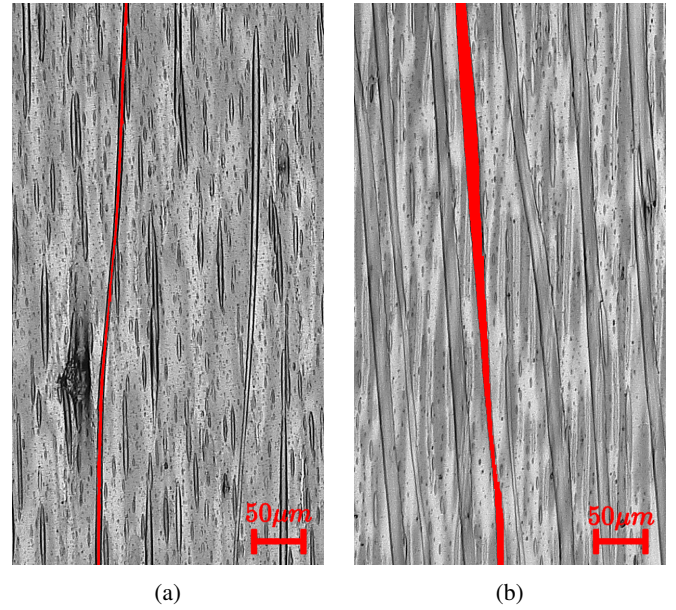


Figure 6: Optical microscopy images of linear nanoparticle aggregates formed with an applied parallel magnetic field during drying of a drop of toluene with a mixture of PS(89.6)-*b*-PB(226) and magnetic PS-coated γ -Fe₂O₃ nanoparticles with a toluene relative humidity of (a) 80% and (b) nominally 100% in the nitrogen gas flow through the STVA chamber. One wire has been highlighted in red for each case, showing that slower solvent evaporation leads to thicker, more densely packed wires.

removal and experiencing dipolar interactions which with application of the parallel magnetic field favor end-to-end chaining. As these chains grow they exceed the spacing between neighboring PS microdomains (cylinder center-to-center spacing ≈ 130 nm, determined from GISAXS (not shown)), enabling aggregates to bridge multiple domains and coalesce into continuous linear assemblies, in agreement with the mechanism reported by Yao et al.⁶.

This experiment confirms that our STVA chamber allows for control of drying rates and promotes reorganization of nanoparticles embedded in a BCP thin film with an applied magnetic field during drying. In this specific case, PS-coated γ -Fe₂O₃ nanoparticles self-assemble into wire-like structures growing from cylinder microdomains in the PS-*b*-PB BCP matrix.

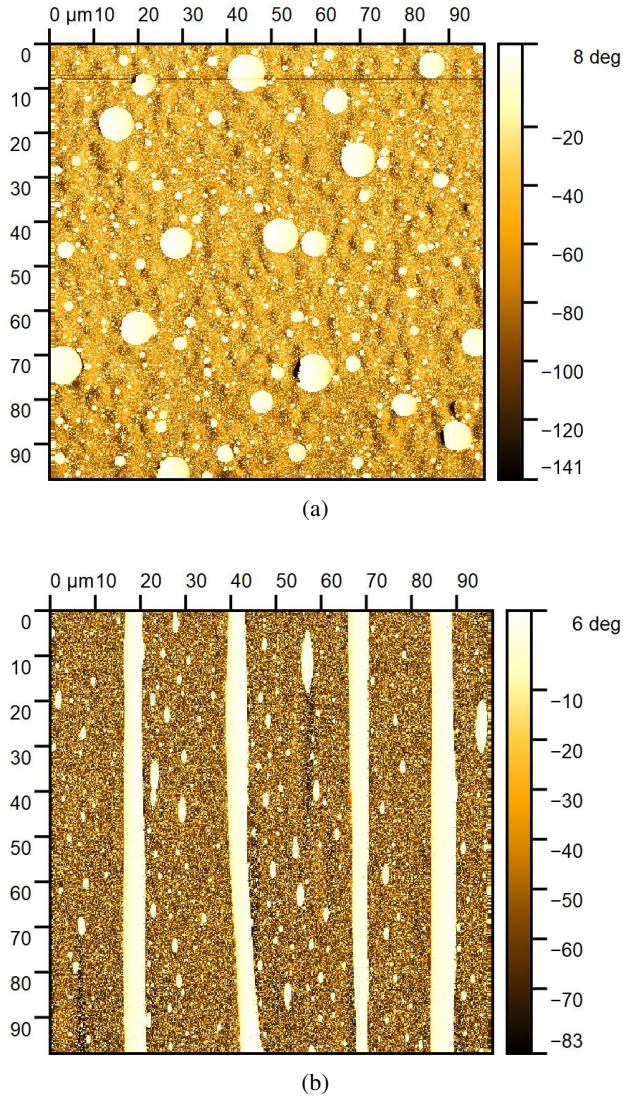


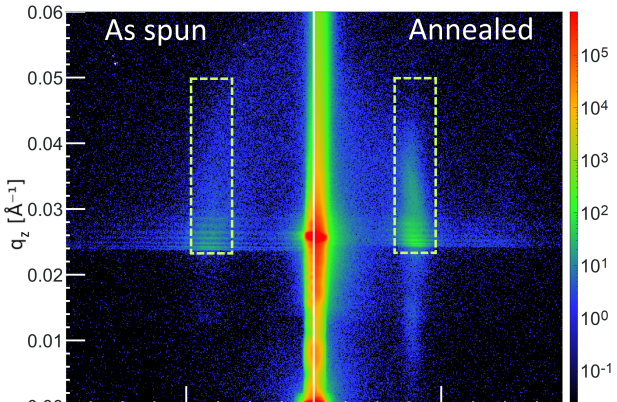
Figure 7: Phase contrast AFM images after drying a drop of toluene with a mixture of PS(89.6)-*b*-PB(226) and magnetic γ -Fe₂O₃ nanoparticles in an atmosphere of nitrogen saturated with toluene: (a) with no magnetic field applied during drying, showing a random nanoparticle aggregate distribution; and (b) with ~ 100 mT parallel magnetic field applied during drying, showing continuous linear assemblies, aligned in the direction of the applied field. In both images, the lighter, larger features correspond to aggregated nanoparticles, whereas the darker, speckled regions correspond to the underlying polymer matrix.

B. STVA and *ex situ* GISAXS of a di-BCP thin film

A 3 wt% PS(21.7)-*b*-PB(60) di-BCP in toluene was spin-coated onto a Si wafer and subjected to 4 h of room-temperature solvent vapor annealing in the STVA chamber with 80% toluene humidity in the nitrogen flow through the chamber. The *ex situ* GISAXS map was measured for 15000 s before and after annealing with an incidence angle of 0.18° (in the dynamical regime between di-BCP and substrate critical

angles), and is shown in Fig. 8a. From the relative size of the two polymer blocks, the BCP is expected to show an ordered structure with PS cylinders in a PB matrix³. Fig. 8a shows one half of each GISAXS map put together. The GISAXS half-map to the left shows a Debye-Scherrer ring indicating randomly oriented cylinders before annealing. The GISAXS half-map to the right indicate the emergence of a 3-dimensional ordered structure of lying cylinders after STVA by the disappearance of the Debye-Scherrer ring and the appearance of an elongated Bragg spot. These observations are emphasized by the presence of a shoulder after STVA in the line cuts along q_z at the q_y position of the lateral peak in the Yoneda band⁴⁰ (the areas in the GISAXS maps used for making these line cuts are marked by rectangles in Fig. 8b). Line cuts along q_y at the q_z position of the Yoneda band (corresponding to the horizontal region marked for another sample in Fig. 11a) show a broad feature after STVA extending in q_y from $\sqrt{3}q_1$ to $2q_1$ (these positions are marked with tics in Fig. 8c), where q_1 is the first-order lateral structural peak, the position of which is found by fitting a Gaussian profile. The occurrence and position of the broad higher-order features are consistent with a hexagonal ordering of the lying cylinders. For a highly ordered structure, we would expect to see peaks rather than shoulders at these positions³⁰. The fact that only broad shoulders and not distinct Bragg peaks are observed suggests that long-range order is still limited in the film.

Phase imaging AFM is consistent with randomly oriented cylinders before STVA (Fig. 9a), while large unidirectional grains are seen to have formed after solvent annealing (Fig. 9b). The Fourier transform of the AFM image of the annealed film indicates preferred domain orientations with hexagonal symmetry in the film surface plane. The same sixfold symmetry is retained in a much larger field-of-view documented in the Supplementary material Fig. S7a, where a minority of standing cylinders near the film surface also are evident. The 'dry' repeat distance has increased after annealing in a 80% toluene humidity atmosphere, from 38.2 ± 0.1 to 41.1 ± 0.1 nm as found from GISAXS maps, and from 41.3 to 44.6 nm found using AFM as shown in Fig. S7b. Both AFM and GISAXS show that annealing in the present case results in an increase of the 'dry' microdomain periodicity which is not uncommon^{52,53} - however, as seen in research example C, the opposite may also be the case. Likewise, it is not surprising that AFM and GISAXS give different values for the microdomain periodicity. In the present case, the GISAXS values which are an average over the whole film depth, are 5-10% lower than the AFM values, which are the microdomain periodicity in the outermost surface layer, where 'reconstruction' due to the polymer-air interface may occur.

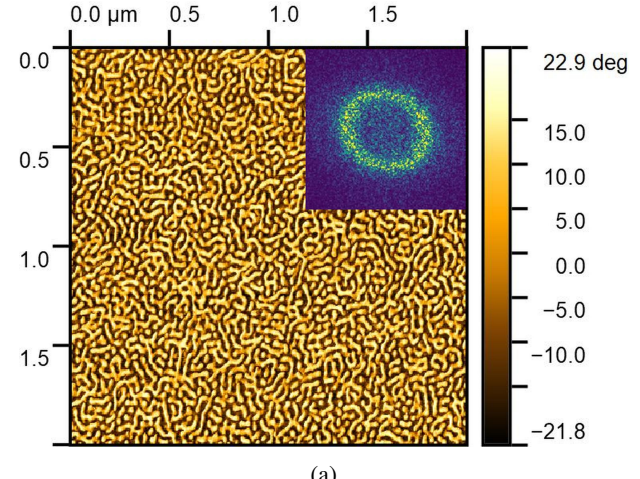


(a)

(b)

(c)

Figure 8: (a) GISAXS maps of PS(21.7)-*b*-PB(60) thin film: unannealed (as-spun) (left) and after 4 h of solvent annealing in a 80% toluene humidity atmosphere (right). The vertical boxed areas indicate the line cuts used in (b). The color scale is in arbitrary units. (b) Summed intensity within the marked vertical box regions plotted along q_z , with curves vertically offset for clarity. Here the shoulder present above 0.03 \AA^{-1} for the annealed film indicates an emerging 3-dimensional ordered structure. (c) Horizontal line cuts at the q_z position corresponding to the Yoneda region. The position of first-order peaks are found by fitting a Gaussian profile. First-order peak positions from these fits are marked by red ticks. Higher-order peak position as expected for hexagonal packing of lying cylinders are marked at $\sqrt{3}q_1$ and $2q_1$ with orange and magenta ticks, respectively.



(a)

(b)

Figure 9: AFM phase images and their Fourier transforms for PS(21.7)-*b*-PB(60) thin films: (a) As-spun film, showing lying cylinders with random in-plane orientations. (b) After 4 h of solvent annealing, where grains of lying cylinders have aligned along preferred in-plane directions. Although the cylinders themselves remain parallel to the substrate, the selection of discrete grain orientations produces an averaged Fourier transform (see inset) with hexagonal symmetry. Cf. Fig. S7a for full-size maps.

C. *In situ* GISAXS on a laboratory instrument during STVA of a BCP thin film

This experiment explores BCP structural reorganizing during STVA at two different temperatures and is performed in the magnetic drawer using dummies in place of magnets, i.e., without application of an external magnetic field. Here, the combinations of annealing temperature and solvent gas flow through the chamber were selected using preliminary calibration runs to iteratively adjust the toluene humidity in the chamber until both annealing temperatures produced the same final equilibrium swelling ratio, i.e., a higher temperature requires

a higher solvent humidity. Polystyrene(38)-*b*-poly(ferrocenyl dimethyl silane)(11) (PDI 1.25) thin film samples were prepared by spin coating a 3 wt% BCP solution in toluene onto Si wafers. The BCPs bulk morphology is expected to consist of poly(ferrocenyl dimethyl silane) spheres arranged on a BBC lattice in a PS matrix⁵⁴. The two as-spun dry films had thicknesses of 110 and 111 nm and were designated for annealing at 25 and 35 °C, respectively. A third control sample with a thickness of 111 nm was prepared under identical conditions and left unannealed. All thicknesses were measured using the spectral reflectometer in the STVA chamber. The two samples were annealed for 4 h and *in situ* GISAXS was used to track the reorganizing of the thin film structure. The equilibrium absorption of toluene vapor was kept the same for the two films annealed at different temperatures by selecting a toluene flow of 0.96 and 1.46 g/h for 25 °C and 35 °C, respectively, resulting in a maximal equilibrium swelling ratio of 1.17 in both cases (see Fig. 11c). The relative toluene humidity in the chamber during annealing was 52% at 25 °C and 48% at 35 °C.

AFM topography images acquired before and after STVA were Fourier transformed. The transforms exhibit diffuse rings characteristic of short-range ordered surface microdomains (See Supplementary Material Fig. S6). These patterns were then azimuthally averaged to produce radial intensity profiles in reciprocal space, $I(k)$ (Fig. 10). Each profile was fitted to a Gaussian plus a Lorentzian function to locate the peak positions, k^* . Calculating the corresponding repeat distances, $d = 1/k^*$, indicates a 50.8 nm repeat distance for the unannealed control sample, while the repeat distances for the samples annealed at 25 and 35 °C were 48.7 and 45.9 nm, respectively. This reduction in repeat distance is investigated further by examining the *in situ* GISAXS data collected during annealing of these samples.

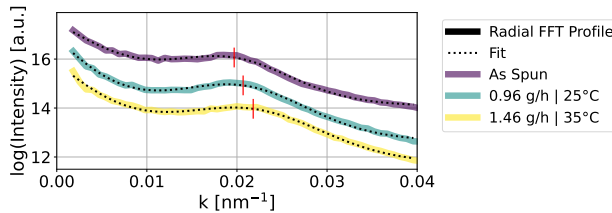


Figure 10: Radial intensity profiles of the Fourier transforms derived from AFM topography images of PS(38)-*b*-PF2MS(11) films before and after solvent annealing in toluene vapor under different conditions (see legend) with summed Lorentzian + Gaussian fits (offset for clarity).

Gaussian peak positions in legend entry order from the top and marked with a red dash on the curves, are 0.0197, 0.0207, and 0.0218 nm^{-1}

Using a laboratory X-ray source necessitates longer exposure times than at a synchrotron source. In the present case, the exposure time was 2028 s for a GISAXS map with a negligible interval between successive exposures measured at an incidence angle of 0.18°. The high electron-density contrast between the iron-rich minority block and the majority block

of the BCP used in this study allows well-developed peaks to be identified in line-cuts, even though features in the corresponding GISAXS maps appear relatively faint. A reduction in the signal-to-noise ratio arises from absorption and parasitic scattering due to the Kapton windows in the beam path. In particular, the Kapton window that separates the sample environment enclosure from the detector vacuum stretches and curves under the one-atmosphere pressure difference, hence adding to the diffuse background.⁵⁵

The spheres formed by the PS minority block are arranged with a characteristic spacing d , giving rise to an intensity maximum located at $q_y = 2\pi/d$ in the Yoneda band. The peak is emphasized by summing the intensity in the horizontal box marked on Fig. 11a. The resulting curve, $I(q_y)$ (Fig. 11b), is fitted to a sum of two Gaussian functions corresponding to the lateral peaks and a Lorentzian function to account for the specular contribution:

$$\log I(q_y) = \sum_{i=1}^2 A_i \exp \left[-\frac{(q_y - q_i)^2}{2\sigma_i^2} \right] + \frac{L_0}{1 + \left(\frac{q_y - q_0}{\Gamma} \right)^2}, \quad (5)$$

where A_i , q_i , and σ_i are the amplitudes, center positions, and widths of the two Gaussians, and L_0 , q_0 , and Γ are the amplitude, center, and half-width at half-maximum of the Lorentzian (Fig. 11b). The uncertainty in d is the standard deviation of the peak positions returned by the fit routine - for the two Gaussians, the average value of d and the corresponding uncertainties are used. Fig. 11c shows that d already in the beginning of the annealing process becomes smaller for the sample annealed at 35 °C compared to the sample annealed at 25 °C (the two samples have the same approximate repeat distance d in the dry state before annealing). This is consistent with the observations from the AFM images, which show a slight decrease in the characteristic distance after annealing, most notably for the sample annealed at 35 °C. However, the repeat distances derived from the AFM images (50.8 nm prior to annealing, 48.7 and 45.9 nm after annealing for 25 and 35 °C, respectively) are systematically higher than the repeat distances obtained with GISAXS (41.6 ± 0.7 and 41.9 ± 1.0 nm prior to annealing and 40.1 ± 0.7 and 39.9 ± 1.0 nm after annealing at 25 and 35 °C, respectively (the GISAXS numbers are found by averaging values from two initial dry GISAXS maps and from two final dry GISAXS maps, respectively)). This difference between AFM and GISAXS results is consistent with the observation in research example B. However, the 'dry' values in the present case are *lower* after annealing than prior to annealing. This result suggests that the final 'dry' microdomain periodicity may depend on the detailed annealing protocol, e.g., with different degrees of strain induced during drying or released during swelling⁸.

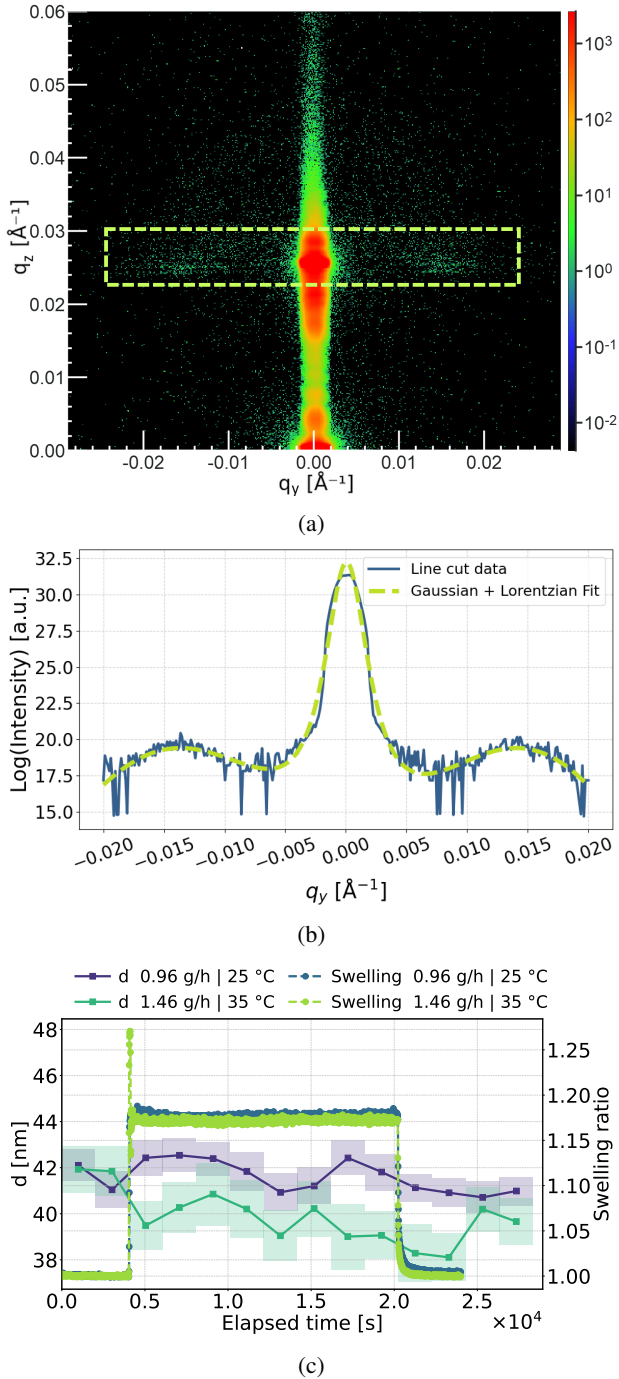


Figure 11: *In situ* GISAXS results during STVA of polystyrene(38)-*b*-poly(ferrocenyl dimethyl silane)(11) thin films. (a) representative GISAXS map during swelling at 25 °C with horizontal line-cut box highlighted. Arbitrary units on the color scale bar for the scattered intensity, (b) A representative graph of data from a line-cut fitted to a sum of two Gaussians and a Lorentzian function (Eq. 5), and (c) The lateral repeat distance resulting from curve fitting as function of time during annealing (with \pm uncertainty marked as a region around the experimental points) at 25 and 35 °C. The corresponding swelling ratio is also plotted.

D. Combined STVA and surface modification using a brush layer

The final example demonstrates the ability of STVA to induce long-range order in combination with the use of brush layers to modify substrate-polymer interactions. The use of brush layers to facilitate block copolymer self-assembly and improve microdomain ordering has previously been demonstrated^{27,56,57}. Here, a brush layer refers to a dense monolayer of short polymer chains covalently grafted, i.e., chemically anchored by one end, to the Si substrate with an oxidized top layer so that the short polymers extend normal to the substrate surface. In our study, three samples were prepared for STVA: two samples with brush layers, one with a PS brush layer and the other with a polydimethylsiloxane (PDMS) brush layer, and one sample without any brush layer. For the two samples designated for brush layer grafting, plasma oxidation (air) of the Si substrate was used to generate surface silanol (Si-OH) groups on the native oxide layer for the ω -hydroxyl end groups of the PS or PDMS chains to covalently anchor to. Immediately afterward, the substrates were spin-coated with a 1 wt% toluene solution of ω -hydroxyl terminated PS (2.2 kg/mol) or PDMS (5 kg/mol). These samples were subsequently annealed under vacuum at 150 °C for 15 h. Following thermal annealing and brush layer formation, a thin film of PS(28)-*b*-PDMS(85) was spin-coated with a 1.5 wt% solution in toluene onto each substrate yielding films with a total approximate thickness of 35 nm. The control film was similarly spin-coated onto an untreated Si wafer. Subsequently, the thin films were solvent-annealed at RT for 2 h at 80% toluene humidity. Cylindrical morphology is expected for this BCP sample³.

AFM topography images were used to characterize the microdomain ordering for each sample. The control sample without a brush layer exhibited limited ordering both as-spun (Fig. 12a) and after solvent vapor annealing (Fig. 12b). Samples with PS and PDMS brush layers showed similarly limited ordering in their as-spun states (Figs. 12c and 12e, respectively). After solvent vapor annealing, however, distinct hexagonal arrangements of standing cylinders emerged in both brush-layer samples, as evidenced by the Fourier transform insets (Figs. 12d and 12f). These results demonstrate that brush layers substantially enhance ordering in thin BCP films, *in casu* PS-*b*-PDMS thin films, but that solvent annealing is required for this ordering to occur.

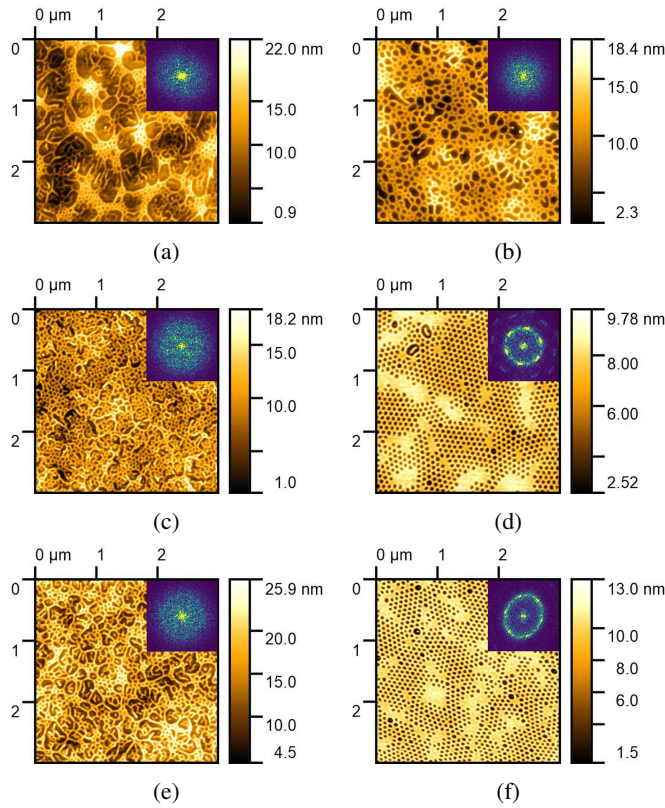


Figure 12: AFM topography images of 35 nm-thick PS(28)-*b*-PDMS(85) films on Si substrates with and without use of a brush layer. Insets are 2-D Fourier transforms of the corresponding images. (a) control sample, no brush layer, as-spun; (b) control sample, no brush layer, after STVA; (c) with PS brush layer, as-spun; (d) with PS brush layer, after STVA; (e) with PDMS brush layer, as-spun; (f) with PDMS brush layer, after STVA. Hexagonal order, indicated by the six-fold symmetry in the Fourier transform, is observed only in the annealed films using a PS or PDMS brush layer (d, f).

V. CONCLUSION

A compact, modular environmental control setup has been developed and validated. It integrates control of solvent vapor humidity in the chamber, temperature regulation, application

of adjustable magnetic fields, and is applicable for GISAXS studies - *in situ* and *ex situ*. The modularity of the design facilitates straightforward sample exchange and reconfiguration for instance when swapping standard drawers with magnetic-field drawers. Evaluations of the chamber performance, including fill and quench times and magnetic field distributions by Gauss meter measurements and confirmed by FEM simulations, demonstrate that the setup enables advanced thin film studies.

The setup is transportable and can be used at both laboratory and synchrotron X-ray sources. Only minor hardware changes are required for other scattering modes: replacing the Kapton windows with thin aluminum foils possibly together with a sample stage accomodating larger samples, can be used to adapt the set-up for GISANS, whereas simply adding a sample mount to the existing stage suffices for transmission SAXS.

The broad utility of the setup is demonstrated with four examples covering use of the magnetic-field stage to align magnetic nanoparticles in a BCP matrix during annealing; *ex situ* GISAXS of a di-BCP thin film before and after STVA showing the creation of long-range order after annealing; *in situ* GISAXS study of the influence of STVA solvent humidity and annealing temperature on the restructuring of a di-BCP thin film and finally the use of STVA to obtain order in a di-BCP thin film when combining with brush layer surface modification. Overall, the versatile setup has a large potential for use in engineering of thin film nanoscale structures and hence in e.g., photonics, nanolithography, as sensors and in membrane and filtration technologies.

ACKNOWLEDGMENTS

We thank Jonathan M. Gow, Ib Høst Pedersen, Rolf Skjold-birk Rønne, Oliver V. Trasbo Madsen, Johnny Faust, Bjarne Christensen, all Roskilde University, for valuable input to the design and use of the STVA setup. Christian Kjeldbjerg was supported by the Danish Committee for Scientific Infrastructure (NUFI) through the ESS Lighthouse "Q-MAT: Magnetism and Quantum Materials". The Novo Nordisk Foundation is gratefully acknowledged for funding RUCSAXS – Roskilde University Interdisciplinary X-ray Scattering Hub – with grant NNF21OC0068491.

The authors have no conflicts of interest to disclose.

¹ Shri Singh, "Phase transitions in liquid crystals," *Physics Reports* **324**, 107–269 (2000).

² John F. Nagle and Stephanie Tristram-Nagle, "Structure of lipid bilayers," *Biochimica et Biophysica Acta (BBA) - Reviews on Biomembranes* **1469**, 159–195 (2000).

³ Frank S. Bates and Glenn H. Fredrickson, "Block copolymer thermodynamics: Theory and experiment," *Annu. Rev. Phys. Chem.* **41**, 525–557 (1990).

⁴ Manesh Gopinadhan, Prashant Deshmukh, Youngwoo Choo, Pawel W. Majewski, Olgica Bakajin, Menachem Elimelech, Rajeswari M. Kasi, and Chinedum O. Osuji, "Thermally switchable

aligned nanopores by magnetic-field directed self-assembly of block copolymers," *Advanced Materials* **26**, 5148–5154 (2014).

⁵ W.-X Fang, Z.-H He, X.-Q Xu, Z.-Q Mao, and H Shen, "Magnetic-field-induced chain-like assembly structures of Fe₃O₄ nanoparticles," *Europhys. Lett.* **77**, 68004 (2007).

⁶ Yuan Yao, Ezzeldin Metwalli, Martin A. Niedermeier, Matthias Opel, Chen Lin, Jing Ning, Jan Perlich, Stephan V. Roth, and Peter Müller-Buschbaum, "Nano- and microstructures of magnetic field-guided maghemite nanoparticles in diblock copolymer films," *ACS Appl. Mater. Interfaces* **6**, 5244–5254 (2014).

⁷ Armin Knoll, Robert Magerle, and Georg Krausch, "Phase be-

havior in thin films of cylinder-forming aba block copolymers: Experiments,” *The Journal of Chemical Physics* **120**, 1105–1116 (2004).

⁸ Christophe Sinturel, Marylène Vayer, Michael Morris, and Marc A. Hillmyer, “Solvent vapor annealing of block polymer thin films,” *Macromolecules* **46**, 5399–5415 (2013).

⁹ Dorthe Posselt, Jianqi Zhang, Detlef-M. Smilgies, Anatoly V. Berezkin, Igor I. Potemkin, and Christine M. Papadakis, “Restructuring in block copolymer thin films: In situ GISAXS investigations during solvent vapor annealing,” *Progress in Polymer Science* **66**, 80–115 (2017).

¹⁰ Zhenyu Di, Dorthe Posselt, Detlef-M. Smilgies, and Christine M. Papadakis, “Structural rearrangements in a lamellar diblock copolymer thin film during treatment with saturated solvent vapor,” *Macromolecules* **43**, 418–427 (2009).

¹¹ Kevin W. Gotrik, Adam F. Hannon, Jeong Gon Son, Brent Keller, Alfredo Alexander-Katz, and Caroline A. Ross, “Morphology control in block copolymer films using mixed solvent vapors,” *ACS Nano* **6**, 8052–8059 (2012).

¹² Jillian A. Emerson, Daniel T. W. Toolan, Jonathan R. Howse, Eric M. Furst, and Thomas H. Epps, “Determination of solvent–polymer and polymer–polymer Flory–Huggins interaction parameters for poly(3-hexylthiophene) via solvent vapor swelling,” *Macromolecules* **46**, 6533–6540 (2013).

¹³ Kevin W. Gotrik and C. A. Ross, “Solvothermal annealing of block copolymer thin films,” *Nano Letters* **13**, 5117–5122 (2013).

¹⁴ Xiaodan Gu, Ilja Gunkel, Alexander Hexemer, Weiyin Gu, and Thomas P. Russell, “An in situ grazing incidence x-ray scattering study of block copolymer thin films during solvent vapor annealing,” *Advanced Materials* **26**, 273–281 (2013).

¹⁵ A. Sepe, P. Černoch, P. Štěpánek, E.T. Hoppe, and C.M. Papadakis, “Creation of lateral structures in diblock copolymer thin films during vapor uptake and subsequent drying – effect of film thickness,” *European Polymer Journal* **50**, 87–96 (2014).

¹⁶ Jong Min Kim, YongJoo Kim, Woon Ik Park, Yoon Hyung Hur, Jae Won Jeong, Dong Min Sim, Kwang Min Baek, Jung Hye Lee, Mi-Jeong Kim, and Yeon Sik Jung, “Eliminating the trade-off between the throughput and pattern quality of sub-15 nm directed self-assembly via warm solvent annealing,” *Advanced Functional Materials* **25**, 306–315 (2014).

¹⁷ Alessandro Sepe, Jianqi Zhang, Jan Perlich, Detlef-M. Smilgies, Dorthe Posselt, and Christine M. Papadakis, “Toward an equilibrium structure in lamellar diblock copolymer thin films using solvent vapor annealing – an in-situ time-resolved GISAXS study,” *European Polymer Journal* **81**, 607–620 (2016).

¹⁸ Gunnar Nelson, Chloe S. Drapes, Meagan A. Grant, Ryan Gnabasik, Jeffrey Wong, and Andrew Baruth, “High-precision solvent vapor annealing for block copolymer thin films,” *Micro-machines* **9**, 271 (2018).

¹⁹ Katherine Evans and Ting Xu, “Self-assembly of supramolecular thin films: Role of small molecule and solvent vapor annealing,” *Macromolecules* **52**, 639–648 (2018).

²⁰ Hanna Hulkkonen, Turkka Salminen, and Tapiro Niemi, “Automated solvent vapor annealing with nanometer scale control of film swelling for block copolymer thin films,” *Soft Matter* **15**, 7909–7917 (2019).

²¹ Mingchao Ma, Runze Liu, Tingyu Su, Zehao Sun, and Caroline A. Ross, “Reversible morphology locking via metal infiltration in a block copolymer,” *ACS Nano* **17**, 12225–12233 (2023).

²² Anja Stenbock-Fermor, Armin W. Knoll, Alexander Böker, and Larisa Tsarkova, “Enhancing ordering dynamics in solvent-annealed block copolymer films by lithographic hard mask supports,” *Macromolecules* **47**, 3059–3067 (2014).

²³ Xiao Cheng, Alexander Böker, and Larisa Tsarkova, “Temperature-controlled solvent vapor annealing of thin block copolymer films,” *Polymers* **11**, 1312 (2019).

²⁴ Mikhail Yu. Efremov and Paul F. Nealey, “Ellipsometry-based combination of isothermal sorption-desorption measurement and temperature programmed desorption technique: A probe for interaction of thin polymer films with solvent vapor,” *Review of Scientific Instruments* **89** (2018).

²⁵ Connor R. Bilchak, Shivajee Govind, Guillermo Contreas, Boris Rasin, Shawn M. Maguire, Russell J. Composto, and Zahra Fakhraai, “Kinetic monitoring of block copolymer self-assembly using ¹³C NMR spectroscopic ellipsometry,” *ACS Macro Lett.* **9**, 1095–1101 (2020).

²⁶ Sungnam Kim, Gumhye Jeon, Sung Woo Heo, Hye Jeong Kim, Seung Bin Kim, Taihyun Chang, and Jin Kon Kim, “High aspect ratio cylindrical microdomains oriented vertically on the substrate using block copolymer micelles and temperature-programmed solvent vapor annealing,” *Soft Matter* **9**, 5550 (2013).

²⁷ Saman Safari Dinachali, Wubin Bai, Kun-Hua Tu, Hong Kyoon Choi, Jinshuo Zhang, Melissa E Kreider, Li-Chen Cheng, and Caroline A. Ross, “Thermo-solvent annealing of polystyrene-polydimethylsiloxane block copolymer thin films,” *ACS Macro Letters* **4**, 500–504 (2015).

²⁸ Cian Cummins, Parvaneh Mokarian-Tabari, Pascal Andreazza, Christophe Sinturel, and Michael A. Morris, “Solvothermal vapor annealing of lamellar poly(styrene)-block-poly(d,L-lactide) block copolymer thin films for directed self-assembly application,” *ACS Appl. Mater. Interfaces* **8**, 8295–8304 (2016).

²⁹ Kyunginn Kim, Sungmin Park, Yeongsik Kim, Joona Bang, Cheolmin Park, and Du Yeol Ryu, “Optimized solvent vapor annealing for long-range perpendicular lamellae in PS-b-PMMA films,” *Macromolecules* **49**, 1722–1730 (2016).

³⁰ Anatoly V. Berezkin, Florian Jung, Dorthe Posselt, Detlef-M. Smilgies, and Christine M. Papadakis, “In situ tracking of composition and morphology of a diblock copolymer film with GISAXS during exchange of solvent vapors at elevated temperatures,” *Advanced Functional Materials* **28** (2018), 10.1002/adfm.201706226.

³¹ E. Bhoje Gowd, Tadanori Koga, Maya K. Endoh, Kamlesh Kumar, and Manfred Stamm, “Pathways of cylindrical orientations in PS-b-P4VP diblock copolymer thin films upon solvent vapor annealing,” *Soft Matter* **10**, 7753–7761 (2014).

³² Michelle A. Chavas, Detlef-M. Smilgies, Ulrich B. Wiesner, and Christopher K. Ober, “Widely tunable morphologies in block copolymer thin films through solvent vapor annealing using mixtures of selective solvents,” *Advanced Functional Materials* **25**, 3057–3065 (2015).

³³ James A. Dolan, Karolina Korzeb, Raphael Dehmel, Karl C. Gödel, Morgan Stefk, Ulrich Wiesner, Timothy D. Wilkinson, Jeremy J. Baumberg, Bodo D. Wilts, Ullrich Steiner, and Ilja Gunkel, “Controlling self-assembly in gyroid terpolymer films by solvent vapor annealing,” *Small* **14** (2018).

³⁴ S. Ariaee, B. Jakobsen, I. H. Pedersen, T. S. Rasmussen, and D. Posselt, “Solvothermal vapor annealing setup for thin film treatment: A compact design with in situ solvent vapor concentration probe,” *AIP Advances* **13**, 065226 (2023).

³⁵ Christopher M. Bates and Frank S. Bates, “50th anniversary perspective: Block polymers—pure potential,” *Macromolecules* **50**, 3–22 (2016).

³⁶ Damian A. Hajduk, Paul E. Harper, Sol M. Gruner, Christian C. Honeker, Gia Kim, Edwin L. Thomas, and Lewis J. Fetter, “The gyroid: A new equilibrium morphology in weakly segregated diblock copolymers,” *Macromolecules* **27**, 4063–4075 (1994).

³⁷ Sangwoo Lee, Michael J. Bluemle, and Frank S. Bates, “Discovery of a frank-kasper σ phase in sphere-forming block copolymer melts,” *Science* **330**, 349–353 (2010).

³⁸ I.W. Hamley, "Ordering in thin films of block copolymers: Fundamentals to potential applications," *Progress in Polymer Science* **34**, 1161–1210 (2009).

³⁹ Florian A. Jung, Anatoly V. Berezkin, Tim B. Tejsner, Dorthe Posselt, Detlef-M. Smilgies, and Christine M. Papadakis, "Solvent vapor annealing of a diblock copolymer thin film with a nons-selective and a selective solvent: Importance of pathway for the morphological changes," *Macromolecular Rapid Communications* **41** (2020).

⁴⁰ P. Müller-Buschbaum, "A basic introduction to grazing incidence small-angle x-ray scattering," in *Applications of Synchrotron Light to Scattering and Diffraction in Materials and Life Sciences* (Springer Berlin Heidelberg, 2009) p. 61–89.

⁴¹ Detlef-M. Smilgies, "Gisaxs: A versatile tool to assess structure and self-assembly kinetics in block-copolymer thin films," *J. Polym. Sci.* **60**, 1023–1041 (2022).

⁴² Cy M. Jeffries, Jan Ilavsky, Anne Martel, Stephan Hinrichs, Andreas Meyer, Jan Skov Pedersen, Anna V. Sokolova, and Dmitri I. Svergun, "Small-angle x-ray and neutron scattering," *Nature Reviews Methods Primers* **1** (2021), 10.1038/s43586-021-00064-9.

⁴³ P. Busch, M. Rauscher, D.-M. Smilgies, D. Posselt, and C. M. Papadakis, "Grazing-incidence small-angle x-ray scattering from thin polymer films with lamellar structures - the scattering cross section in the distorted-wave born approximation," *Journal of applied crystallography* **39**, 433–442 (2006).

⁴⁴ Rémi Lazzari, "Isgisaxs: a program for grazing-incidence small-angle x-ray scattering analysis of supported islands," *Journal of Applied Crystallography* **35**, 406–421 (2002).

⁴⁵ H. Angus Macleod, *Thin-Film Optical Filters* (CRC Press, 2010).

⁴⁶ CSC – IT Center for Science, "Elmer fem solver," <https://www.csc.fi/elmer>, accessed 4 February 2025.

⁴⁷ Magnet-Shop GmbH, "Neodymium block magnet 30.0 x 10.0 x 5.0 mm n40 nickel holds 6.5 kg," <https://www.magnet-shop.com/neodymium/blockmagnets/blockmagnet-30.0-x-10.0-x-5.0-mm-n40-nickel-holds-6.5-kg> (2025), accessed October 2025.

⁴⁸ Frank Hartmann, Martin Bitsch, Bart-Jan Niebuur, Marcus Koch, Tobias Kraus, Christian Dietz, Robert W. Stark, Christopher R. Everett, Peter Müller-Buschbaum, Oliver Janka, and Markus Gallei, "Self-assembly of polymer-modified FePt magnetic nanoparticles and block copolymers," *Materials* **16**, 5503 (2023).

⁴⁹ Magdalena Konefał, Peter Černoch, Vitalii Patsula, Ewa Pavlova, Jiří Dybal, Karol Załęski, and Alexander Zhigunov, "Enhanced ordering of block copolymer thin films upon addition of magnetic nanoparticles," *ACS Appl. Mater. Interfaces* **13**, 9195–9205 (2021).

⁵⁰ Nan Zhu, Haining Ji, Peng Yu, Jiaqi Niu, M. U. Farooq, M. Waseem Akram, I. O. Udego, Handong Li, and Xiaobin Niu, "Surface modification of magnetic iron oxide nanoparticles," *Nanomaterials* **8**, 810 (2018).

⁵¹ V. Cabuil, N. Hochart, R. Perzynski, and P. J. Lutz, "Synthesis of cyclohexane magnetic fluids through adsorption of end-functionalized polymers on magnetic particles," in *Trends in Colloid and Interface Science VIII*, Progress in Colloid and Polymer Science, Vol. 97, edited by R. H. Ottewill and A. R. Rennie (Steinkopff, Heidelberg, Germany, 1994) Chap. 15, pp. 71–74.

⁵² Jianqi Zhang, Dorthe Posselt, Detlef-M. Smilgies, Jan Perlich, Konstantinos Kyriakos, Sebastian Jakusch, and Christine M. Papadakis, "Lamellar diblock copolymer thin films during solvent vapor annealing studied by gisaxs: Different behavior of parallel and perpendicular lamellae," *Macromolecules* **47**, 5711–5718 (2014).

⁵³ Ilja Gunkel, Xiaodan Gu, Zhiwei Sun, Eric Schaible, Alexander Hexemer, and Thomas P. Russell, "An in situ gisaxs study of selective solvent vapor annealing in thin block copolymer films: Symmetry breaking of in-plane sphere order upon deswelling," *Journal of Polymer Science Part B: Polymer Physics* **54**, 331–338 (2015).

⁵⁴ Rob G. H. Lammertink, *Poly(ferrocenyldimethylsilanes) at the Interface of Chemistry and Materials Science: Synthesis, Structure-Properties and Thin Film Applications*, Ph.D. thesis, University of Twente, Enschede, The Netherlands (2000).

⁵⁵ M. Antimonov, A. Khounsary, S. Weigand, J. Rix, D. Keane, J. J. Grudzinski, A. Johnson, Z. Zhou, and W. Jansma, "Large-area kapton x-ray windows," in *Proc. SPIE*, Vol. 9588 (2015) p. 95880F.

⁵⁶ Yeon Sik Jung, J. B. Chang, Eric Verploegen, Karl K. Berggren, and C. A. Ross, "A path to ultranarrow patterns using self-assembled lithography," *Nano Letters* **10**, 1000–1005 (2010).

⁵⁷ Amir Tavakkoli K. G., Adam F. Hannon, Kevin W. Gotrik, Alfredo Alexander-Katz, Caroline A. Ross, and Karl K. Berggren, "Rectangular symmetry morphologies in a topographically templated block copolymer," *Advanced Materials* **24**, 4249–4254 (2012).